A novel non convex sparse recovery method for single image super-resolution, denoising and iterative MR reconstruction

Nishant Zachariah[1], Johannes M Flake[2], Qiu Wang[3], Boris Mailhe[3], Justin Romberg[1], Xiaoping Hu[4], and Mariappan Nadar[3]

[1]Department of Electrical and Computer Engineering, Georgia Institute of Technoloy, Atlanta, GA, United States, [2]Department of Mathematics, Rutgers University, New Brunswick, NJ, United States, [3]Imaging and Computer Vision, Siemens Corporate Technology, Princeton, NJ, United States, [4]Department of Biomedical Engineering, Emory University and Georgia Institute of Technology, Atlanta, GA, United States

INTRODUCTION: In this work, we develop a novel generic non convex framework which outperforms (quantitatively and qualitatively) state of the art algorithms for super-resolution, image denoising and iterative MR reconstruction. In each of the three applications we explored in this work (super-resolution, denoising and under sampled iterative image reconstruction), the developed method captures clinically relevant features and reconstructs these features with the highest fidelity thereby aiding in the clinical diagnostic process.

METHODS: *Super-resolution:* The MRI single image super-resolution can be formulated as a sparse non convex signal recovery functional. The goal is to recover the high resolution image ($x \in \mathbb{C}^{n\,x\,1}$) when only the low resolution image ($y \in \mathbb{C}^{m\,x\,1}$) has been observed through the system point spread function ($B \in \mathbb{C}^{n\,x\,n}$) and the resulting loss in resolution($D \in \mathbb{C}^{m\,x\,n}$) operator. The non convex sparse prior is imposed as a pseudonorm regularizer ($\|\ \|_p$), where $0 < p < 1$. The optimization problem takes the form$\min_{x \in \mathbb{C}^{n\,x\,1}} \left(\lambda \|Wx\|_p + 1/2\, \|DBx - y\|_2^2\right)$. We solve this optimization problem using a proximal splitting framework and benchmark our super-resolution results against the state of the art non convex solver SARA[1], L1 solver FISTA[2] and super-resolution algorithms published in[3-4]. It must be noted that that application of SARA for super-resolution is novel in and of itself but is not the focus of this work. *Denoising:* The MRI image denoising problem requires the injection on a smoothness prior which takes form of either an isotropic or anisotropic total variation regularizer. The optimization problem is stated as$\min_{x \in \mathbb{C}^{n\,x\,1}} \left(\lambda \|Wx\|_p + 1/2\, \|DBx - y\|_2^2 + \|TV(x)\|\right)$. We use a parallel proximal splitting method to solve this optimization problem. We quantify our results using the peak signal to noise ratio metric. For image denoising, we compare our results to state of the art denoising techniques [5-7]. We quantify our denoising results using the image quality metric. *Compressed Sensing:* For compressed sensing reconstruction, the D, B operators are replaced by a partial Fourier operator. We benchmark IAN's reconstruction against the non convex solver SARA [1], L1 solver FISTA [2] and L2 based gradient descent. We quantify our results using both the peak signal to noise ratio (PSNR) metric and the structural similarity index (SSIM).

RESULTS: We herein refer to our novel algorithm which solves the non convex optimization problem as IAN. *Super-resolution:* In Fig. 1 we demonstrate IAN's ability to super-resolve relevant clinical margins of tumor in the temporal lobe. Numerically IAN outperforms SARA by 1.92dB and all other competing methods by a minimum mean square error improvement factor of 3. Visually, IAN reconstructs the tumor margins with the greatest fidelity as evidenced by the residual plot shown in the bottom panel of Fig. 1. We also include additional numerical results for super-resolution of a scaphoid fracture and denoising of a ground truth noisy knee image (Table 1) (images not shown). In each of these cases, IAN performs quantitatively and qualitatively better than the state of the art competing method. *Denoising:* In Fig 2. we use IAN with TV to denoise a naturally noisy MRI image. Table 1, summarizes the quantitative reconstruction results for denosing including images not presented here. *Compressed Sensing:* In Fig 3. we use IAN reconstruct a cardiac image by significantly under sampling k-space. We demonstrate that IAN is able to reconstruct the under sampled acquisition with the highest fidelity relative to competing methods. SARA produces comparable results to IAN in the compressive reconstruction case (however with lower SSIM relative to IAN).

DISCUSSION: From the presented quantitative results in Table 1 and from the qualitative results presented in Fig. 1-3, it is clear that IAN out performs the state of the art non convex, convex and even dedicated application specific algorithms for super-resolution, denoising and iterative image reconstruction. The algorithmic architecture of IAN was intentionally developed in a manner that is parallelizable across GPU / CPU cores for efficient practical implementation. Empirical examination reveals that IAN is relatively robust to parameter tuning. We have also developed a Monte Carlo based Stein Unbiased Risked Estimator (SURE) to automatically tune the parameters of our algorithm for image denoising applications.

CONCLUSION: We demonstrate that the generic novel non convex framework that we have developed (IAN), can be used to solve a wide array of image processing challenges. IAN outperforms the gold standard algorithms in single image super-resolution, denoising and under sampled iterative MR reconstruction (compressed sensing). Furthermore, we have designed IAN's software architecture to be intrinsically parallel in order to ensure efficient integration into existing MR image reconstruction software. Given the generic formulation that IAN seeks to solve, it can be adapted in the future for use in applications such as image inpainting (recovery of occluded field of view in medical images) or blind deconvolution where the parameters of the point spread function are unknown.

REFERENCES – [1] R. Carrillo et al Mon. Not. of the Roy. Astro. Soc, 426(2), 1223–1234, 2012. [2] A. Beck et al, SIAM J. on Imag Sci, (2)1, 183–202, 2009. [3] S. Mallat et al, Imag Proc, IEEE Trans on, 19(11), 2889–2900, 2010 [4] W. Dong, et al, Imag Proc, IEEE Trans on, 22(2), 700–711, 2013 [5] A. Beck et al, Imag Proces, IEEE Trans on, 18(11), 2419–2434, 2009 [6] K. Dabov, et al, Imag Proc, IEEE Trans on, 16(8), 2080–2095, 2007 [7] P. Chatterjee et al, Imag Proc, IEEE Trans on, 21(4), 1635–1649, 2012

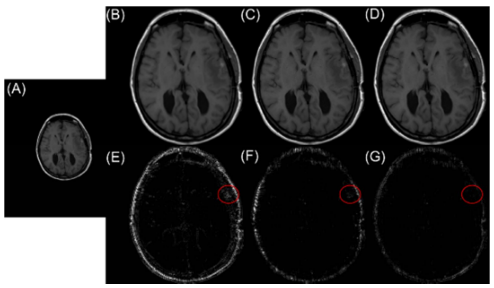

Figure 1: Single Image Super-resolution results for temporal tumor. (A) Observed low resolution blurry image (B) Image recovered using the method of sparse mixing estimators (C) Image recovered using SARA (D) Image recovered using IAN. (E) Image residual for SME relative to ground truth (F) SARA residual (G) IAN residual. Red Circle indicates location of the tumor. IAN has the least residual error in the clinical region of interest. Quantitative results are in Table 1

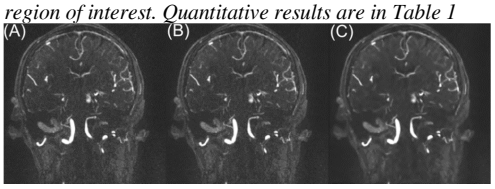

Figure 2: MRI ground truth image denoising for a patient with a cerebral aneurysm. (A) Original noisy image (B) Image denoised using BM3D (C) Image denoised using IAN with TV. IAN with TV has eliminated most of the rician noise generated in the MRI image acquisition process (Table 1)

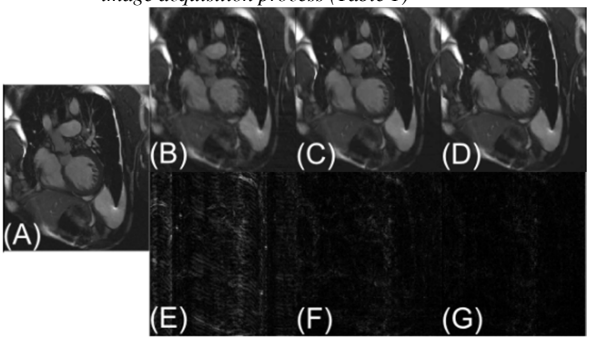

Figure 3: Image reconstruction from compressive data acquisition. (A) Ground truth (B) L2 gradient descent reconstruction (PSNR: 35.71 dB, SSIM 0.924) (C) L1 FISTA reconstruction (PSNR: 39.25 dB, SSIM: 0.954) (D) Non Convex IAN reconstruction (PSNR: 42.44 dB, SSIM: 0.972). (E) Gradient descent residual (F) L1 FISTA residual (G) IAN residual. IAN has the least residual error (G)

Table 1 : Superresolution and Denoising Results

		Super-resolution Method				
Image Type	**Metric**	SME[3]	SAIST[4]	FISTA[2]	SARA[1]	IAN
Tumor	PSNR	40.31	30.29	44.61	45.05	**47.02**
Angiography	PSNR	34.66	31.21	37.43	37.65	**38.65**
Scaphoid	PSNR	26.45	24.86	26.88	27.32	**27.80**
		Image Denoising Method				
Image Type	**Metric**	SARA[1]	FGP[5]	PLOW[7]	BM3D[6]	IAN
Aneurysm	IQM	-0.215	0.234	0.408	0.571	**0.715**
Knee	IQM	-0.276	0.487	0.374	0.438	**0.543**